Studies of laser-plasma interaction physics with low-density targets for direct-drive inertial confinement fusion on the Shenguang III prototype SCI F

V. T. Tikhonchuk,[1,2,a] T. Gong,[3] N. Jourdain,[1] O. Renner,[1,4] F. P. Condamine,[1] K. Q. Pan,[3] W. Nazarov,[5]
L. Hudec,[6] J. Limpouch,[6] R. Liska,[6] M. Krůs,[4] F. Wang,[3] D. Yang,[3] S. W. Li,[3] Z. C. Li,[3]
Z. Y. Guan,[3] Y. G. Liu,[3] T. Xu,[3] X. S. Peng,[3] X. M. Liu,[3] Y. L. Li,[3] J. Li,[3] T. M. Song,[3] J. M. Yang,[3]
S. E. Jiang,[3] B. H. Zhang,[3] W. Y. Huo,[7] G. Ren,[7] Y. H. Chen,[7] W. Zheng,[7] Y. K. Ding,[7] K. Lan,[7,8] and S. Weber[1,9]

AFFILIATIONS

[1]ELI-Beamlines, Institute of Physics, Czech Academy of Sciences, 25241 Dolní Břežany, Czech Republic
[2]Centre Lasers Intenses et Applications, University of Bordeaux–CNRS–CEA, 33405 Talence, France
[3]Laser Fusion Research Center, China Academy of Engineering Physics, Mianyang 621900, China
[4]Institute of Plasma Physics, Czech Academy of Sciences, 18200 Prague, Czech Republic
[5]Independent Foam Target Supplier, Carnoustie, DD7 6DP, United Kingdom
[6]Faculty of Nuclear Sciences and Physical Engineering, Czech Technical University in Prague, 11519 Prague, Czech Republic
[7]Institute of Applied Physics and Computational Mathematics, Beijing 100088, China
[8]Center for Applied Physics and Technology, Peking University, Beijing 100871, China
[9]School of Science, Xi'an Jiaotong University, Xi'an 710049, China

Note: This paper is part of the Special Issue on Progress in Matter and Radiation at Extremes in China.
[a]**Author to whom correspondence should be addressed:** vladimir.tikhonchuk@eli-beams.eu

ABSTRACT

The physics of laser-plasma interaction is studied on the Shenguang III prototype laser facility under conditions relevant to inertial confinement fusion designs. A sub-millimeter-size underdense hot plasma is created by ionization of a low-density plastic foam by four high-energy (3.2 kJ) laser beams. An interaction beam is fired with a delay permitting evaluation of the excitation of parametric instabilities at different stages of plasma evolution. Multiple diagnostics are used for plasma characterization, scattered radiation, and accelerated electrons. The experimental results are analyzed with radiation hydrodynamic simulations that take account of foam ionization and homogenization. The measured level of stimulated Raman scattering is almost one order of magnitude larger than that measured in experiments with gasbags and hohlraums on the same installation, possibly because of a greater plasma density. Notable amplification is achieved in high-intensity speckles, indicating the importance of implementing laser temporal smoothing techniques with a large bandwidth for controlling laser propagation and absorption.

I. INTRODUCTION

A comprehensive understanding of parametric instabilities and the possibility of controlling them in the context of inertial confinement fusion (ICF) remains a challenging task. The details of the absorption processes and the detrimental effects of hot electrons on the implosion process are of great importance for both direct and indirect implosion schemes. At the moment, there are no reliable methods of controlling parametric instabilities and there is a serious risk of their adverse effects preventing ignition conditions from being reached. There is a clear need for more experimental studies

supported by theoretical analysis and simulations. Here, we present results of studies of the excitation of parametric instabilities and generation of hot electrons in an underdense preformed plasma under conditions relevant to ICF implosion experiments with spatial scales of 300 μm or more and electron temperatures in the region of 2 keV. The experiments are performed on the Shenguang III prototype (SGIII-P) laser facility delivering about 8 kJ energy at a wavelength of 0.35 μm and a pulse duration of a few nanoseconds.[1–3]

A large number of experiments have been performed on different laser facilities at a sub-kilojoule energy level, but they have involved smaller characteristic plasma lengths and lower temperatures.[4–8] The competition between stimulated Raman scattering (SRS) and two-plasmon decay (TPD) near a quarter critical density[9] depends strongly on the electron temperature,[10–12] and it is important to generate temperatures in the range of 2 keV–3 keV in order to assess their behavior under fusion-related conditions. Moreover, excitation of stimulated Brillouin scattering (SBS) and its competition with SRS[13–18] in a plasma with density below quarter critical depends on the plasma temperature and density scale length. For these parameters to be comparable to those under ICF conditions, a laser energy of several kilojoules is needed for the plasma creation.

Several experiments have already been conducted at the multi-kilojoule laser energy level[3,19–21] and have provided important information about the nonlinear laser–plasma interaction. They have been conducted in a planar geometry, which provides access to various diagnostics for plasma characterization and measurements of nonlinear processes. The use of low-density foams[22] in the experiments[19,23] is advantageous because of the possibility of creating a quasi-homogeneous high-temperature plasma with small velocity gradients.[24] However, numerical simulations of foam ionization are difficult. It is known that the ionization front propagates inside a foam sample more slowly than in a homogeneous material of equivalent density and chemical composition. Several models have been proposed recently of how this delay can be treated numerically,[25–30] and it is also important to compare them with experiments.

In the present paper, we report on an experiment dedicated to studies of laser-plasma interaction under conditions relevant to ICF with low-density foam targets. The preliminary experimental design has been described in Ref. 31.

The remainder of the article is organized as follows. Numerical simulations of plasma formation from a foam under the experimental conditions are presented in Sec. II. Section III describes the experimental setup and diagnostics. Section IV presents the major experimental results and their qualitative analysis. A discussion and conclusions are presented in Sec. V.

II. NUMERICAL MODELING OF LASER-PLASMA INTERACTION

A. Interaction conditions

We aim for studies of laser-plasma interactions under conditions relevant to ICF. A large-scale ($L_n \sim 300\,\mu$m), underdense ($n_e \sim 0.2 n_{cr}$), and hot ($T_e \sim 2$ keV) plasma was created with four laser beams delivering a total energy of 3.2 kJ in 1 ns at the third harmonic ($\lambda = 0.351\,\mu$m) of a Nd:glass laser. Here, L_n is the plasma density scale length, n_e and T_e are the electron density and temperature, λ is the laser wavelength, and $n_{cr} = 9.05 \times 10^{21}$ cm^{-3} is the corresponding critical density. Four laser beams irradiated from two sides a foam

target of average density 10 mg/cm^3–12 mg/cm^3 and thickness 0.8 mm, and then, with a time delay of 0.5 ns or 1 ns, an interaction laser beam at the same wavelength and with intensity close to 10^{15} W/cm^2 was used for the interaction studies.

B. Hydrodynamic simulations

Plasma formation was simulated using radiation hydrodynamic codes with the goal of defining the optimal interaction conditions, that is, creation of a sufficiently homogeneous plasma with required density and temperature.

The experiment is three-dimensional, and it cannot be fully simulated using the available hydrodynamic codes accounting for the laser-plasma interaction and foam structure. Consequently, the numerical simulations were performed in two steps. First, interaction of heating beams with the target was simulated using the two-dimensional (2D) axisymmetric Eulerian radiation hydrodynamic code XRL2D,[32,33] which describes laser energy deposition accurately but models foam as a homogeneous material. Second, the propagation of the ionization front in the foam was simulated using the 2D axisymmetric arbitrary Lagrangian–Eulerian hydrodynamic code PALE (Prague Arbitrary Lagrangian Eulerian),[34] which accounts for the foam's porous structure but considers normal incidence of laser beams. To make the simulations compatible with these two codes, the laser power in the PALE simulation was adjusted to obtain the same ionization front velocity as in the XRL2D simulation with the same homogeneous material.

XRL2D is a 2D Eulerian radiation hydrodynamic code for studying laser interactions with solid-density targets. The electron and ion energy equations are solved with Kershaw's nine-point diffusion difference scheme, and the electron heat flux is determined by the flux-limited diffusion model. The radiation transfer equation is solved by the flux-limited multigroup diffusion method. The laser energy deposition via inverse bremsstrahlung is calculated with a 3D ray-tracing package. The thermodynamic quantities are derived either from the ideal gas model or from data on the realistic equation of state. The mean opacity is calculated with the relativistic self-consistent average atom model OPINCH,[35] and contributions from free-free, free-bound, and bound-bound transitions are taken into account.
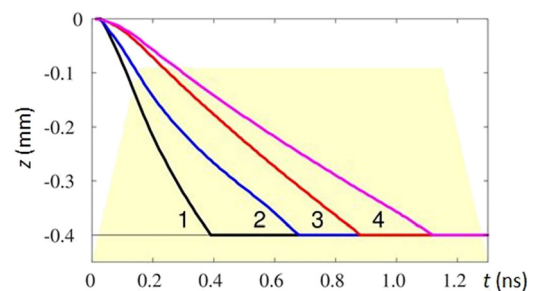

FIG. 1. Time dependence of the ionization front position in hydrodynamic simulations of the target considered as a homogeneous material of density 10 mg/cm^3 (1) and 12 mg/cm^3 (2) and with a model[29] accounting for the foam homogenization with foam density 10 mg/cm^3 (3) and 12 mg/cm^3 (4). The yellow background shows the temporal profile of the laser pulse power. The laser propagates in the negative z direction, and the foil edge is at $z = 0$.
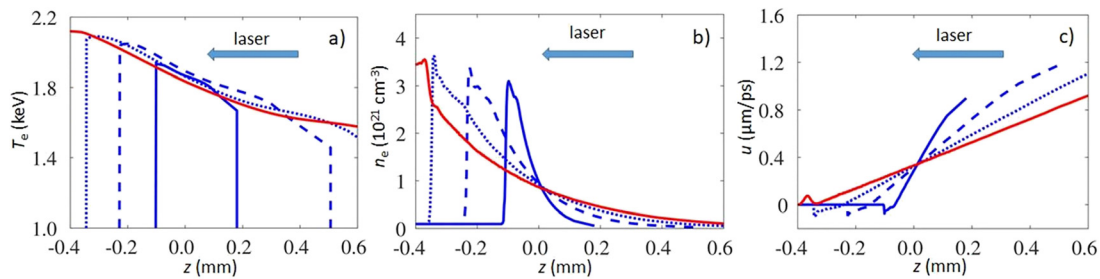
FIG. 2. Spatial profiles of plasma electron temperature (a), density (b), and flow velocity (c) at four time moments of 0.25 ns (solid blue), 0.5 ns (dashed blue), 0.75 ns (dotted blue), and 1 ns (solid red) calculated using the PALE code for a foam density of 10 mg/cm³. The laser propagates in the negative z direction, and the foil edge is at z = 0.

In the XRL2D simulations, two laser beams incident on a target from one side at an angle of 45° were modeled using a cone of opening angle of 45° with respect to the target normal and at a realistic power, and the target was modeled as a homogeneous material of equivalent density. Such a simulation describes the delivered laser energy correctly, but unfortunately does not account for the foam homogenization and thus overestimates the plasma temperature and ionization front velocity. Figure 1 shows the position of the ionization front as a function of time along the target normal. The simulations with a target described as a homogeneous material (curves 1 and 2) overestimate the ionization front velocity.

The propagation of an ionization front in a foam is delayed because of the time needed for dense elements in the foam to expand under the heat flux delivered by the laser beam, electrons, or radiation. Depending on the foam density and the laser intensity and wavelength, the ionization may propagate as a fast supersonic ionization wave or as a blast hydrodynamic wave including density compression beyond the front. Among the different numerical descriptions of foam homogenization,[27–29] we implemented in our 2D axisymmetric hydrodynamic code PALE the hydrothermal wave model described in Ref. 29 and enhanced by random scattering of the laser light in the nonhomogenized foam region.

PALE[34] is a hydrodynamic Lagrangian code for laser-generated plasma simulations. It solves hydrodynamic Euler equations for mass, momentum, and energy conservation laws, accounts for the Spitzer–Härm flux-limited electron heat conductivity, and assumes normal incidence of the laser light. It describes laser propagation and energy deposition by a ray tracing model including inverse bremsstrahlung and resonance absorption at the critical surface. The state of the plasma is described by the quotidian equation of state (QEOS).[36]

A degree of foam homogenization ISFOAM is calculated for each macroscopic computational cell following the foam model established by Gus'kov et al.[37] ISFOAM is zero for fully homogenized cells, equals one for cells with a cold foam, and is between zero and one for cells undergoing homogenization. This parameter determines the major macroscopic properties of a foam material,[29] such as laser absorption, electron heat conduction, and hydrodynamic motion. The hydrothermal wave model is complemented by ray scattering from randomly oriented foam elements. When a ray enters the computational cell, it is randomly scattered with a probability equal to IsFoam of the cell.

The results of the simulations for foam densities of 10 mg/cm³ and 12 mg/cm³ are shown in Fig. 1. The ionization front was detected as the position where the electron temperature attained a value of 200 eV, which is sufficiently large compared with the cold material, but still about 10

times smaller than the maximum temperature in the heated plasma. The front velocity is delayed, and the calculated value of the front velocity of 350 μm/ns–450 μm/ns was used for choosing the foam thickness. The foam of thickness of 0.8 mm was expected to be ionized in 1 ns while being irradiated by laser beams from two sides. Unfortunately, the ionization front velocity observed in the experiment was smaller than expected, about 300 μm/ns–350 μm/ns, and so the foam was not fully ionized.

The numerical simulation with the PALE code was used for defining the plasma hydrodynamic parameters of the expanding hot plasma and characterization of the parametric instabilities. The plasma characteristics along the symmetry axis for the foam density of 10 mg/cm³ are shown in Fig. 2. The plasma temperature is nearly constant in space and in time, with a characteristic value of $T_e \simeq 1.8$ keV. The positions of the ionization and rarefaction fronts are clearly defined by an abrupt increase in temperature. The profiles of the expansion velocity are approximately linear, as expected for an isothermal rarefaction wave. The stationary point is located near the plasma edge, $z = 0$, where the flow velocity is equal to the acoustic velocity $c_s \simeq 350$ μm/ns. The characteristic spatial scale of velocity variation increases linearly with time, attaining a value $L_u \simeq 300$ μm at $t = 1$ ns.

The electron density profile shown in Fig. 2(b) is nearly exponential, with a characteristic scale increasing linearly with time and with a characteristic value $L_n \simeq 300$ μm at the end of the heating pulse. A small density compression above the full ionization value of 3.2×10^{21} cm⁻³ can be seen near the ionization front. However, in the close vicinity of the ionization front, the plasma density is too steep, and so parametric instabilities can develop farther from the front where the plasma density decreases below 2×10^{21} cm⁻³, that is, below a quarter critical density, $\frac{1}{4}n_{cr} = 2.26 \times 10^{21}$ cm⁻³.

The temporal dependence of the scattered light calculated using PALE is shown in Fig. 3 for the laser interaction with the 10 mg/cm³ foam. The total scattered energy amounts to about 13% of the incident energy of the heating laser beams. The strongest scattering occurs at the very beginning of the laser pulse, when the foam is not yet ionized. When the ionization wave is formed and propagates inside the foam, the intensity of scattered radiation decreases with time, because of laser light absorption in the ionized plasma. As the foam solid elements are randomly oriented, the light scattering contains a small diffusive component.

III. EXPERIMENTAL SETUP AND DIAGNOSTICS

A. Experimental setup and targets

The overall scheme of the experimental setup and plasma diagnostics is shown in Fig. 4. In the experiments, we used five laser
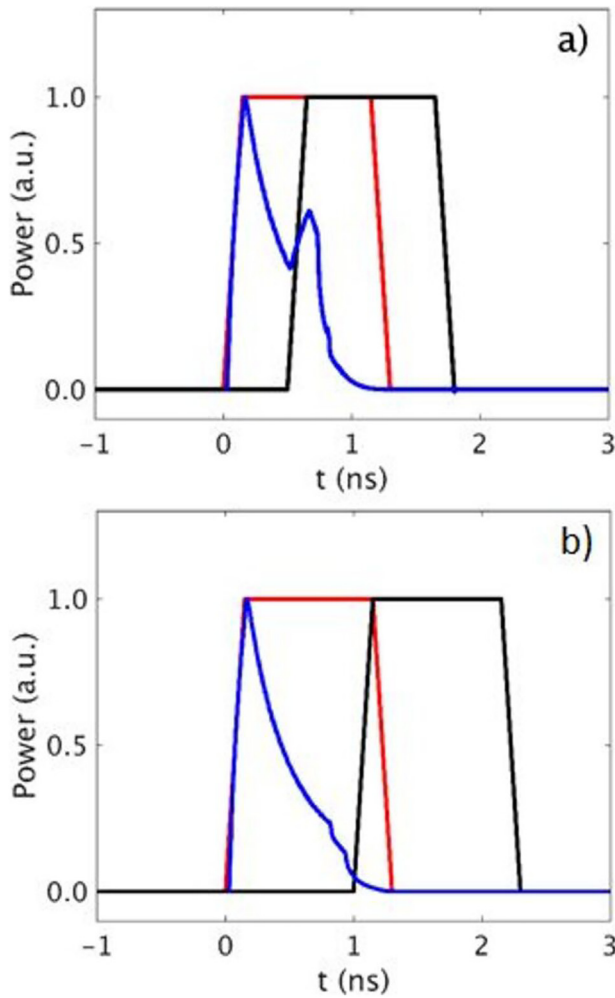
FIG. 3. Temporal dependence of the fraction of scattered light (blue) obtained in the PALE simulation for a foam density of 10 mg/cm², with the heating laser beams (red) and with the interaction laser beam (black) delayed by 0.5 ns (a) and 1 ns (b). All pulses are normalized to unity.

beams at the Shenguang-III prototype laser facility.[1–3] Each beam delivered ~800 J at the third harmonic (wavelength 351 nm) in a trapeze-like pulse of 1 ns duration with a rise and fall time of 0.15 ns. All the beams had an elliptical shape so that their footprints on the target surface were circular. Four laser beams were used for the plasma creation. As shown in Fig. 5, they were focused from two sides on the target at an angle of 45° with respect to the normal with an f/5.4 focusing lens. Beams S1 and S2 came from the top hemisphere and beams S3 and S4 from the bottom. Each pair of beams was focused 250 μm below the corresponding target surface in a circle of diameter 500 μm. The beam transverse profile was super-Gaussian of order 3.5, more than 90% of energy was contained within this circle, and the overlapping intensity of two beams was 8×10^{14} W/cm². The interaction beam N2 had the same energy, but it was focused to a spot of 300 μm diameter with the same super-Gaussian transverse profile and

arrived at a delay of 0.5 ns or 1 ns with respect to the heating beams. The intensity on target of this beam was $(1.0–1.2) \times 10^{15}$ W/cm².

All laser beams were smoothed spatially with continuous phase plates and temporally by spectral dispersion (SSD). The laser pulse spectral width at the wavelength of 351 nm was 0.02 Å without SSD and 1 Å with SSD. Temporal smoothing was switched off for the interaction beam N2 in several shots, with the goal of evaluating the role of high-intensity speckles in the excitation of parametric instabilities.

As shown in Figs. 5 and 6(a)–6(c), the beams did not overlap at the upper target surface. The interaction beam propagated about 200 μm through the cold foam before entering the hot plasma created by the heating beams. This represents less than 20% of the total target volume crossed by the interaction beam. Moreover, analysis of the Kα images presented in Sec. IV D implies that interaction takes place throughout the beam trajectory in the plasma. Thus, the role of nonionized foam is expected to be small.

The targets were made of a foam with a density of 10 mg/cm³ or 12 mg/cm³ and a pore size of ~1 μm and were doped with copper nanoparticles at a mass fraction of 1% for diagnostic purposes. The foam chemical formula $C_{15}H_{20}O_6$ corresponds to a maximum electron density of 3.2×10^{21} cm⁻³ (for the foam mass density of 10 mg/cm³) with ions having average charge $Z = 3.85$ and average atomic mass $A = 7.2$. This density is approximately one-third of the critical density, which is $n_{cr} = 9.05 \times 10^{21}$ cm⁻³ for a laser wavelength of 0.351 μm. The foam of diameter 2 mm was supported by a washer of diameter 8 mm with a 1.2 mm window for x-ray diagnostics, as shown in Fig. 6(d). The foam thickness of 0.8 mm was chosen from the expected ionization front velocity, which was about 400 μm/ns for our laser parameters according to the numerical simulations presented in Sec. II.

While the quarter critical density was produced near the ionization front, numerical simulations presented in Sec. II show that the density profile is too steep in this region, and parametric instabilities cannot be excited at densities above 0.2 n_{cr}. This is in agreement with the optical measurements presented in Sec. IV C, which do not show any activity near quarter critical density.

B. Diagnostics

Scattered light from the plasma was measured with two full-aperture backscattering (FABS) stations installed on the beams S1 and N2, and with a near-backward-scattering (NBS) station installed on the beam N2. The FABS measured signals in two spectral domains, near the main laser wavelength (denoted by SBS) and downshifted (denoted by SRS), within the laser beam focusing aperture of ~0.03 sr, with temporal resolution better than 100 ps and spectral resolution better than 0.1 nm in the SBS channel and better than 10 nm in the SRS channel.

The NBS station collected the light scattered outside the laser focusing cone within a solid angle of 0.30 sr. The scattered light was collected by a hollowed off-axis ellipsoidal mirror and then separated into two channels by a beam splitter for SBS and SRS measurements, respectively. In the SBS channel, the detectable wavelength was in the range 351 ± 2 nm; in the SRS channel, the detectable wavelengths ranged from 400 nm to 700 nm. In each channel, the scattered light was recorded by an energy meter, without temporal resolution.
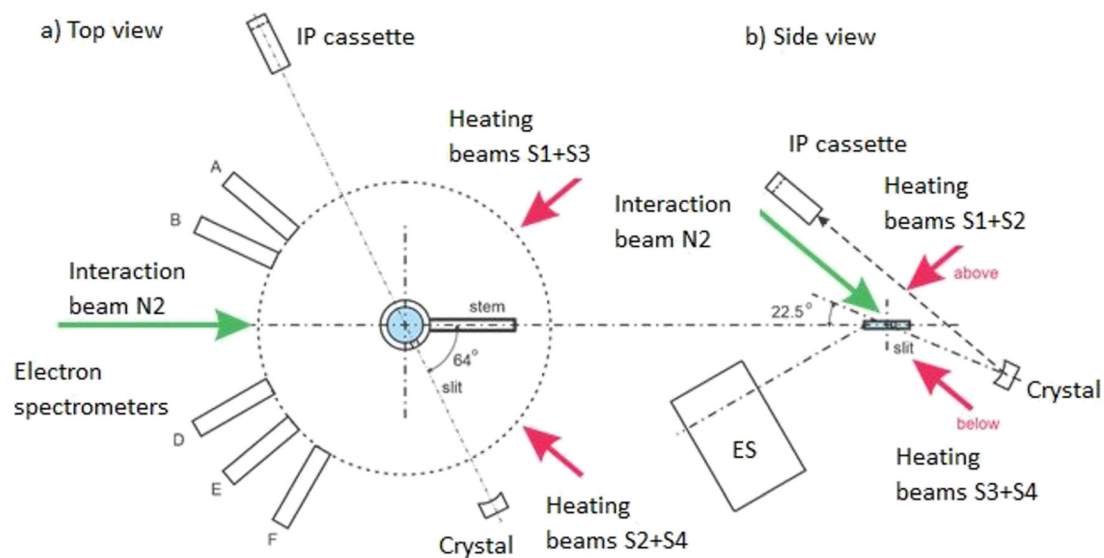
FIG. 4. Overall experimental setup seen from the top (a) and the side (b). Red arrows indicate the direction of incidence of the heating beams S1–S4, and green arrows indicate the direction of the interaction beam N2. The target and the washer are in the target chamber center. The positions of the electron spectrometers (ES) are indicated by letters A, B, D, E, and F. Also shown are the positions of the crystal and a cassette with image plates (IP) for the Kα detection.

The x-ray diagnostics were operated in the hard and soft spectral ranges. Their position with respect to the target laser beams is shown in Fig. 4. A Kα imager was used to observe the plasma from the right side in Fig. 4(b) at an angle of 22.5° with respect to the target plane. Photons were reflected from the crystal and detected at the image
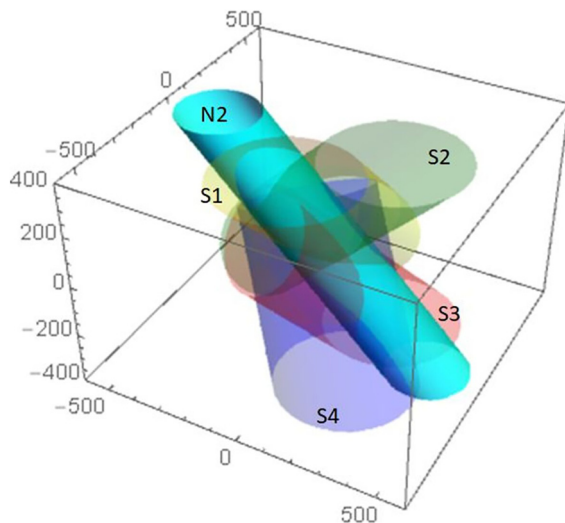

FIG. 5. Scheme of overlapping of the heating and interaction beams in the foam target. The heating beams S1 and S2 and the interaction beam N2 come from the top and the heating beams S3 and S4 from the bottom. All beams are directed at an angle of 45° with respect to the target normal. The beams S1 and S2 are focused 150 μm above the target center, the beam N2 is focused at the center, and the beams S3 and S4 are focused 150 μm below the target center.

plate (IP) protected by filters of Mylar, aluminum, and copper. The imager was absolutely calibrated and measured Kα emission with energies 8046 eV–8050 eV of the cold copper atoms (with temperature less than 120 eV and ionization state $Z^* < 15$[38]) excited by energetic electrons having energy above 9 keV. The detection efficiency was 1.3×10^{-6} per photon emitted from the target assuming isotropic emission. This accounts for the solid angle of view of the crystal of 3.2×10^{-3} sr (see Fig. 4), its reflectivity, spectral acceptance (0.8 mÅ), IP resolution, and sensitivity.

A soft x-ray spectrometer (SXS) measured the spectrum of soft emission of the plasma at an angle of 20° from the target normal in the upper hemisphere. Soft x rays were measured by 15 channels, which covered the energy range from 125 eV to 4000 eV with a resolution ranging from 40 eV to 50 eV at the bottom edge to 100 eV–200 eV at the top edge. This setup has a better resolution in the energy range below 1000 eV and a poorer resolution above 1000 eV. The x-ray spectra were obtained by iterative fitting of the signals recorded by the 15 channels and by comparison with the theoretically predicted spectra.

An x-ray streak camera (XSC) provided a time-resolved plasma image in the normal to the target direction. It observed the plasma in soft x rays with a temporal resolution better than 50 ps through the window in the washer as shown in Fig. 6(d). The imaging slit was parallel to the target surface (thus providing spatial resolution between the top and bottom of the target), and then the slit of the XSC itself was perpendicular to the target surface. The XSC measured the position of the ionization fronts as a function of time as they propagated through the foam.

Target self-emission was also measured using two x-ray pin-hole cameras (XPHCs) recording plasma emission in the energy range above 2 keV. One camera (XPHC1) was positioned in the upper hemisphere at an angle of 20° from the target normal, and the other
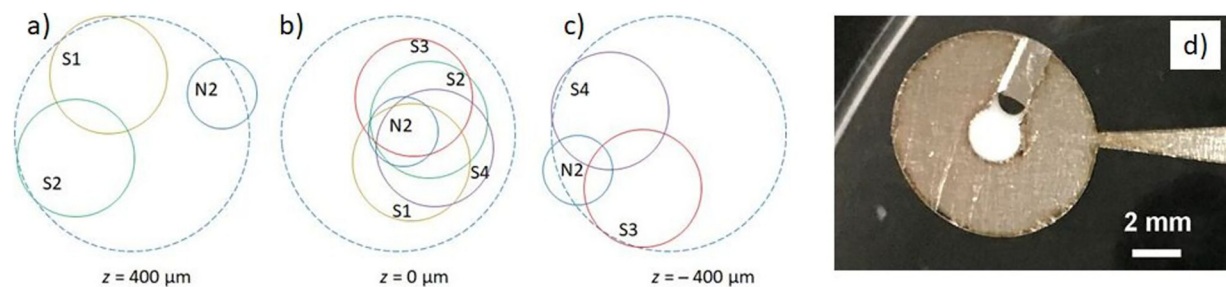
FIG. 6. Footprints of the heating beams and the interaction beam N2: (a) at the top of the foam target, 400 μm from the target center; (b) at the target center; (c) at the bottom, −400 μm from the target center. The blue dashed circles of radius 500 μm are drawn for reference. (d) Photograph of the foam target (white), washer, and holder as used in the experiment.

(XPHC2) saw the target from the lower hemisphere at an angle of 45° with respect to the equatorial plane. XPHC1 was operated in all shots and provided the major information, whereas XPHC2 was operated only in five shots and provided complementary information.

Electron emission outside the targets was monitored by several compact spectrometers (ES) based on fast electron deflection in a magnetic field. In each of these spectrometers, electrons transmitted through an aperture with a diameter of 1 mm drilled in a thick Murytal plastic are affected by a transverse field between steel poles attached to permanent magnets. The optimum distance of the entrance aperture from the target is 300 mm but the construction of spectrometers is flexible enough to guarantee reliable operation at an arbitrary angle and distance from the target. The energy range covered by each spectrometer spans from 55 keV to 1.5 MeV. This energy range is much larger than the plasma potential, which is comparable to the bulk electron temperature and cannot be more than a few keV in our experiment. The trajectories of electrons in the magnetic field are traced using the SIMION code,[39] taking into account the measured field strength. The cross-sections of these trajectories with the plane of the detector, the absolutely calibrated imaging plate BAS-SR, determine the scale for energy distribution measurements of incident electrons.

In the experiment, five electron spectrometers were employed. They were positioned at a distance of 30 cm from the target and observed the plasma from the left hemisphere at an angle of 45° with respect to the equatorial plane and at angles of 65°–80° with respect to the propagation direction of the interaction beam. The solid angle of detection was 10^{-5} sr.

IV. EXPERIMENTAL RESULTS AND QUALITATIVE ANALYSIS

The parameters of the laser beams and targets as well as the overall results obtained with optical and x-ray diagnostics are presented in Table I. There were in total 11 useful shots (numbered from 334 to 344), two of them without interaction beam (335 and 343) and one shot with only two heating beams coming from the top side (341). The laser energy was varied from shot to shot within less than 10%.

The full form of the identification number of each shot is SGIIIP-SHOT2019XXX. In what follows, we retain only the last three digits of the shot number.

A. Observations of laser-plasma interaction in the x-ray domain

An example of the time-integrated spectra obtained with the soft x-ray spectrometer (SXS) in three consecutive shots is shown in Fig. 7(a). It shows Lyα emission of carbon and oxygen ions in the

TABLE I. Characteristics of the laser beams and targets in each shot along with measured optical and x-ray signals. The values in columns N2 show the SBS and SRS signals from the N2 beam only. The energy of a parasitic specular light measured by the N2 FABS station is subtracted from these data. Original data are shown in Table II in the Appendix.

Shot no.	Density (mg/cm³)	Laser energy (J)						Delay (ns)	SSD On N2	N2 SBS (%)		N2 SRS (%)		S1 FABS (%)		Kα (10⁹ photons)	
		S1	S2	S3	S4	N2	Total			FABS	NBS	FABS	NBS	SBS	SRS	Top	Bottom
334	10	795	891	761	806	722	3975	0.5	Off	4.5	8.5	...	11.5	9.2	0.7	...	...
335	10	1026	982	757	807	0	3572	...	...	0	0	...	0	7.9	2.4	...	...
336	12	837	861	810	868	816	4192	0.5	Off	5.4	5.9	...	11.8	8.5	0.4	...	...
337	12	957	838	771	769	754	4089	0.5	Off	9.1	12.2	2.4	16.4	15.2	...	1.45	2.42
338	10	889	912	781	804	801	4187	1.0	Off	4.4	5.9	5.4	28.5	16.4	...	0.13	0.27
339	10	655	751	778	844	698	3726	1.0	On	4.1	3.9	2.2	20.3	8.6	...	0.26	0.13
340	12	916	912	729	754	790	4101	1.0	On	5.7	3.5	2.5	21.2	13.2	...	0.24	0.38
341	12	800	847	0	0	820	2467	1.0	On	6.0	0.3	2.7	20.6	12.0	...	...	...
342	12	930	873	762	737	910	4212	1.0	Off	8.7	−0.9	4.2	17.6	14.1	...	11.6	9.5
343	12	869	870	768	753	0	3260	...	...	0	0	0	0	13.0	...	0.22	0.27
344	10	868	792	770	772	913	4115	1.0	Off	3.1	4.0	0	25.0	12.4	...	...	...

domain below 1 keV and L-shell emission of copper ions near 1.4 keV. The copper L-shell group allows us to estimate the bulk temperature, since the positions of these lines are sensitive to temperature variations in the range from 1 keV to 2 keV.

For shots 338 (blue curve) and 339 (red curve), the Cu group shape is in agreement with the plasma temperature of 1.8 keV calculated with the hydrodynamic code and discussed in Sec. II. For shot 340 (black curve), the bulk temperature is lower. According to the shape of the structure (broader and shifted to low energies), the bulk temperature is of the order of 1 keV. The origin of such a significant temperature variation will be studied in future experiments.

Figure 7(b) shows an image recorded in shot 338 with the x-ray streak camera (XSC). Time goes from top to the bottom and the origin of the x axis is at the target center. There are bright emissions from $x \simeq$ −0.4 mm and +0.4 mm corresponding to the plasma edges. Emission from the left edge is weaker and cut from the top, as it was partially obscured by the positioning mask. The total pulse duration in this shot, including the heating and interaction beams, is 2 ns, but the duration of x-ray emission is longer, as plasma cools and expands after the end of the laser pulse. Unfortunately, the resolution of this XSC image is not sufficiently good, and it is overexposed. Thus, it is difficult to discern the position of the ionization front. This is much better resolved in the image taken in shot 341, where only two heater beams have irradiated the foam from the left side [see Fig. 7(c)]. Here, it is evident that the ionized region is extended to 300 μm–350 μm from the left foam edge to the right during the time of heating beams of 1 ns. There is no ionized plasma from the other side of the foam. So, this figure demonstrates clearly that the ionization front propagates with a velocity of ~300 μm/ns–350 μm/ns, which is less than the ~400 μm/ns expected from the numerical simulations reported in Sec. II. Therefore, we conclude that the foam was not fully ionized by the heating beams. The two ionization waves propagating from both edges of the foam did not converge at the center during the time of heating.

The observed ionization front velocity is of the same order as the ion acoustic velocity of ~300 μm/ns–350 μm/ns calculated with the hydrodynamic code and discussed in Sec. II. Thus, the foam ionization and plasma expansion proceed simultaneously. A rarefaction

wave forms behind the ionization front and produces an inhomogeneous plasma with density scale length increasing in time, as shown in Fig. 2(b).

XPHC images of the target are shown in Fig. 8. They can be compared directly with the beam footprints in Fig. 6. Figures 8(a) and 8(b) taken in two consecutive shots reveal the geometry of interaction. The central bright emission comes from the heating beams S1 (coming from the top) and S2 (coming from the left). The bright spot near the right edge of the blue circle is emission from the interaction beam N2. Emission on the bottom edge of the blue circle in Fig. 8(b) comes from the bottom plasma irradiated by the beam S3. It is disabled in shot 341 and is absent in Fig. 8(a).

The images in Figs. 8(a) and 8(b) were taken with XPHC1. They are only slightly distorted along the vertical axis, with a coefficient cos 20° = 0.94. The image in Fig. 8(c) was taken with XPHC2, and it is more strongly distorted along the vertical axis, with a coefficient cos 45° = 0.71. The interaction beam still comes from the right and the heating beam S3 from the top. These images confirm that all the laser beams were focused on the central part of the target and did not touch the washer. All recorded emissions are thus coming from the foam plasma, which extends outside the beam footprints. The average radius of the plasma column can be estimated to be about 400 μm.

B. Observations of scattered light near the laser frequency

A typical time-resolved spectrum of the scattered light near the laser frequency is shown in Fig. 9(a). As expected from hydrodynamic simulations (see Fig. 3), it has two peaks, corresponding to the heating and interaction pulses. The spectral features corresponding to these two peaks are rather different. The spectral width of the first one is narrow, similar to the laser bandwidth. The second peak is spectrally broadened. Similar features can be seen in the spectra recorded in other shots and shown in Fig. 9(b).

To understand the origin of these emissions, two shots (335 and 343, with foam densities 10 mg/cm^3 and 12 mg/cm^3, respectively) were performed with only four heating beams activated. Both S1 and
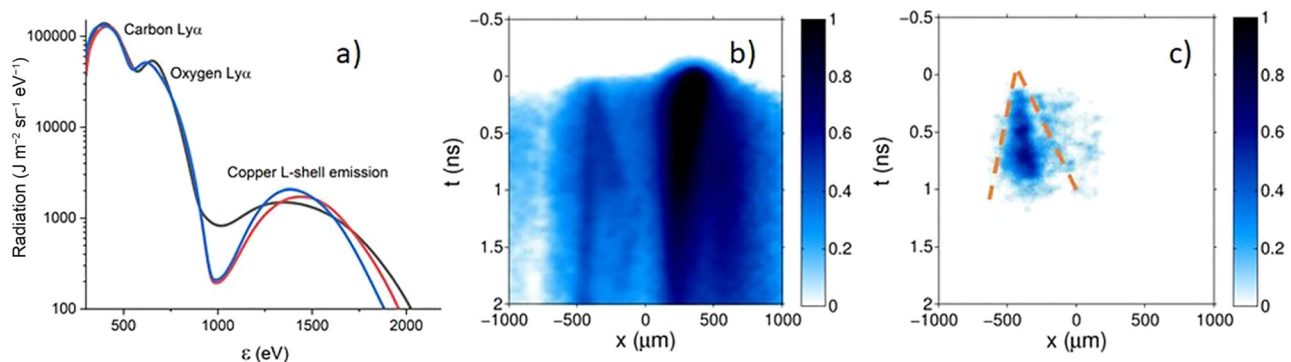

FIG. 7. (a) Spectrum of soft x-ray plasma emission obtained with the SXS diagnostic in three consecutive shots: 338 (blue), 339 (red), and 340 (black). Peaks at 367 eV, 653 eV, and 1400 eV correspond to the emission of carbon, oxygen, and copper ions at a plasma temperature of 1.8 keV. (b) Streaked image of plasma observed with the XSC diagnostic in soft x rays in the equatorial plane through the washer slit in shot 338. The x axis in the image corresponds to the target normal direction, with the point $x = 0$ corresponding to the target center. (c) Streaked image of plasma obtained with XSC in shot 341, where the heating beams S3 and S4 coming from the right were disabled. The orange dashed lines show the putative positions of the ionization front (right) and the expanding plasma (left).
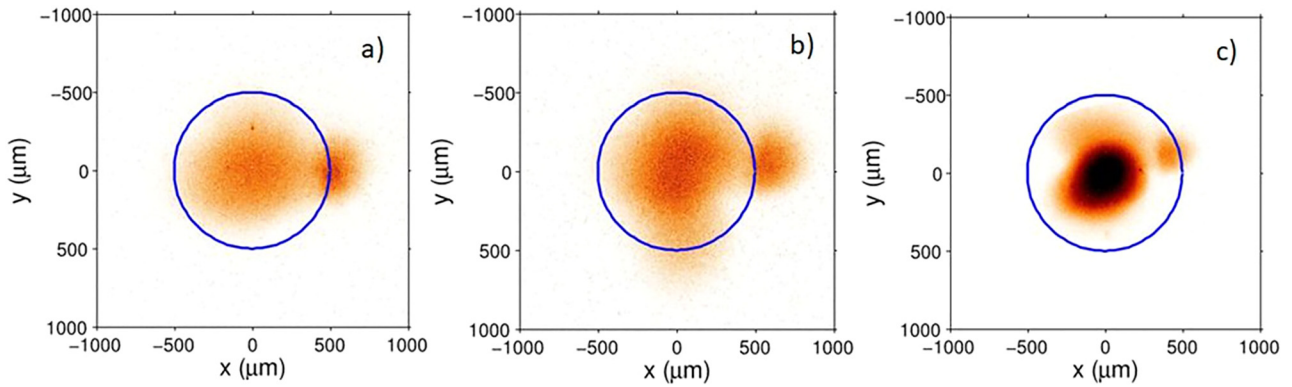
FIG. 8. Hard x-ray pinhole images recorded with XPHC1 [(a) and (b)] and XPHC2 (c) in shots 341 (a) and 342 [(b) and (c)]. The orientation of (a) and (b) is the same as in Fig. 6(a) (the interaction beam N2 comes from the right). In shot 341, the heating beams S3 and S4 were disabled. The blue circles of diameter 1 mm are drawn for reference.

N2 FABS stations were activated and measured nonzero signals. Figure 10(a) shows the temporal profile of the heater beams and the signal near the main wavelength recorded by the N2 FABS station. As shown in Table II in the Appendix, the N2 SBS FABS station measured a significant level of reflectivity of ~9%–16%. While this reflectivity agrees with the levels reported in other experiments,[3,40,41] this early scattered light cannot be produced by SBS from the heating beams, because at these early times the plasma density and velocity profiles are so steep that the SBS gain is much smaller than one. We suppose that these signals originate from specular and diffuse scattering of the heating beams from the cold nonionized foam. The narrow spectrum of scattered light in shot 335, shown by the red curve in Fig. 9(b) confirms this conclusion.

This hypothesis is consistent with the foam homogenization model presented in Sec. II. Similarly to the observation, the calculated scattered signal, shown by the blue curves in Figs. 3(a) and 3(b), is strongest at the beginning of the heating pulse during the first 0.2 ns–0.3 ns and decreases strongly afterwards.

As can be seen from Figs. 5 and 6(a), the line of view of the N2 FABS station corresponds to the direction of specular reflection of the S2 beam. Considering the energy of the S2 beam in shot 335 of 982 J and the energy of 23.7 J measured by N2 FABS, the scattered fraction is 2.4%. To separate the scattered signal produced by the interaction beam, the contribution of this initial parasitic signal was subtracted from the SBS signal recorded by the N2 FABS station in the shots with the interaction beam. A similar procedure was applied to the N2 NBS measurements, where the parasitic specular reflectivity was 9.8%. The data in Table I show already-corrected reflectivities. The columns "N2 SBS" and "N2 SRS" in the table show only the scattered light produced by the N2 beam. This procedure is based on only two laser shots. It may introduce uncontrolled errors, and this may be the reason why the effect of SSD on the reflectivity level is not observed. The original energies measured in the experiment are shown in Table II in the Appendix for reference.

The second burst of backscattered light shown in Figs. 9 and 10(b) is stronger than the first one, and its spectrum is significantly broadened. This cannot be explained by diffuse reflection from the foam, which is expected to be much weaker at that time (see the second maximum of

reflectivity in the numerical simulation in Fig. 3). This burst of backscattering can be explained by excitation of SBS and by its subsequent suppression. Such a process of excitation and self-suppression of SBS has already been observed in Refs. 41 and 42 and has been interpreted as a result of speckle self-focusing and beam spraying.

In our experiment, the laser beam focused with a lens $f_\# = 5.4$ creates speckles with a transverse size $d = f_\# \lambda \simeq 1.9 \ \mu m$ and longitudinal length $z_R = \pi d^2/\lambda \simeq 32 \ \mu m$. For a laser intensity 10^{15} W/cm^2, the average speckle power is about 30 MW, which is a factor of 5–10 smaller than the critical power of ponderomotive self-focusing P_{cr} in a plasma with a temperature of 2 keV and a density of 0.2 n_{cr}. (According to Ref. 43, the critical power can be represented as $P_{cr} \simeq 40 T_{keV} n_{cr}/n_e$ MW, where the electron temperature T_e is in keV.) So, we do not expect speckle self-focusing under our conditions, but excitation of SBS is possible.

The SBS convective gain[43,44] is proportional to the laser intensity and the characteristic length of plasma flow variation L_u. It can be conveniently represented as

$$G_{SBS} = 0.45 I_{15} L_u \lambda_0 T_{keV}^{-1} n_e/n_{cr}, \qquad (1)$$

where the laser intensity I_{15} is in units of 10^{15} W/cm^2 and the characteristic length of velocity variation L_u and the laser wavelength λ_0 are in micrometers. The plasma density and velocity profiles are obtained in the hydrodynamic simulations presented in Sec. II. For the interaction beam average intensity $I_{15} \simeq 10^{15}$ W/cm^2 and for the calculated temperature $T_e \simeq 1.8$ keV, velocity scale length $L_u \simeq 100 \ \mu m$, and density $n_e/n_{cr} \simeq 0.1$–0.2, the expected SBS gain is of the order of $G_{SBS} \simeq 1$–2, and so stimulated scattering from the average laser intensity should not be observed. However, light intensity in speckles is several times larger than the average laser intensity. Theoretical analysis[45–47] shows that a strong SBS backscattering of the order of a few percent can be excited in speckles for the gain calculated for the average intensity of the order of 1. We therefore conclude that scattering from high-intensity speckles is the origin of SBS observed in our experiment.

While speckle self-focusing is not expected under our interaction conditions, the density perturbations produced by the ponderomotive force in speckles propagate across the plasma as ion acoustic waves
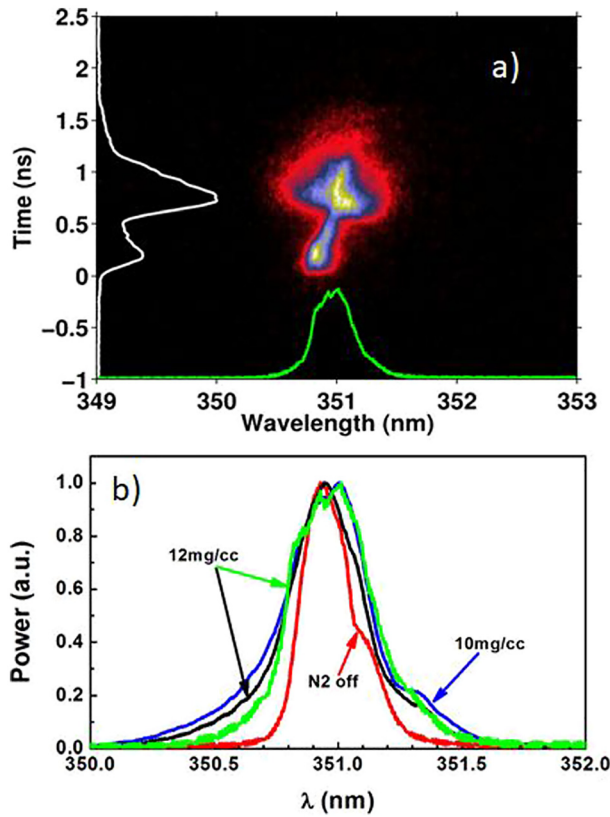
FIG. 9. (a) Time-resolved spectrum of laser light scattered in the N2 FABS near the laser frequency in shot 337. The white and green curves show the time dependence of intensity and the time-integrated spectrum. (b) Time-integrated spectra near the laser wavelength recorded by the N2 FABS station for shots 334 (blue), 335 (red), 336 (black), and 337 (green). In shots 334, 336, and 337, the interaction beam N2 was delayed by 0.5 ns and SSD was turned off; in shot 335, the N2 beam was not activated. The foam density is 10 mg/cm³ in shots 334 and 335, and 12 mg/cm³ in shots 336 and 337.

and produce laser beam refraction and spraying. According to the theoretical analysis by Grech *et al.*,[48] beam spraying may take place for a speckle average power of the order of 5%–10% of the critical power. It is likely that a similar process takes place in our experiment, since the speckle power satisfies that criterion.

The measured level of SBS in the backward direction is of the order of (5.7 ± 1.3)%, and it is not notably affected by the SSD and foam density variation. This is in agreement with the fact that SBS develops on a time scale of a few picoseconds, which is shorter than the laser beam correlation time. The fraction of scattered light detected with NBS is of the same order of magnitude. It varies in a large range from 0% to 12%, with an average value of 6.3%.

The time-integrated spectra of SBS measured with N2 FABS are shown in Fig. 9(b). They are broadened to about 0.3 nm and redshifted with respect to the laser wavelength by less than 0.1 nm. These values are smaller than expected in a plasma at rest. The SBS-driven ion acoustic wave has a frequency $\omega_s \simeq 2\omega_0 c_s/c$, where c is the velocity of light and $c_s \simeq 300\ \mu$m/ns–350 μm/ns is the ion acoustic velocity. That

would correspond to a wavelength shift of about 0.7 nm, which is much larger than observed. Consequently, SBS develops in the transonic zone, where the plasma flow velocity is equal to the local acoustic velocity. This is in agreement with the hydrodynamic simulations shown in Fig. 2(c). This zone corresponds to a plasma density $n_e/n_{cr} = 0.1$ and a large velocity scale length $L_u \sim 100\ \mu$m, which are favorable for SBS development.

C. SRS observations

Time-resolved and time-integrated spectra of downshifted scattered light measured by the N2 FABS station are shown in Fig. 11. The spectrum covers a broad region from 450 nm to 610 nm. It is evident that it is due to SRS. The corresponding density range is $n_e/n_{cr} = 0.05$–0.18. The maximum emission at 510 nm corresponds
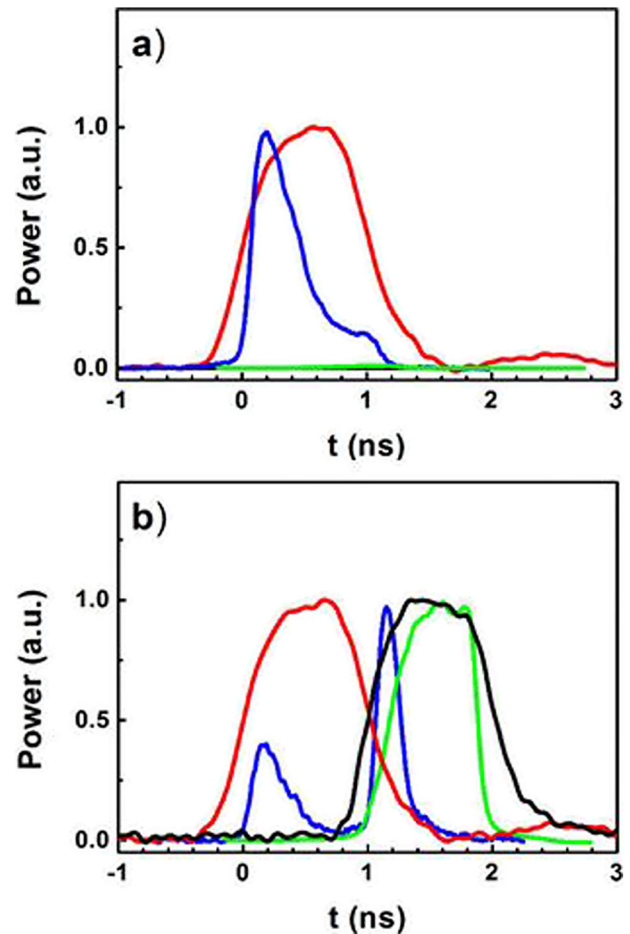

FIG. 10. (a) Temporal profiles of the heating laser beam S1 (red) and the backward-scattered signal (blue and green, in the SBS and SRS channels, respectively) recorded in shot 335 with only four heating beams activated. (b) Temporal profiles of the heating S1 beam (red), the interaction beam N2 (black, delayed by 1 ns), backward-scattered light near the laser frequency (blue), and backward-scattered SRS signal (green) recorded in the 339. All signals were recorded by the N2 FABS station.

to a density $n_e/n_{cr} = 0.1$. According to the hydrodynamic simulation shown in Fig. 2(b), this range of densities corresponds to the foam edge, -0.2 mm $< z < 0.1$ mm. This location of the SRS activity is in agreement with the Kα emission shown in Fig. 12(a).

There is no scattered light near the wavelength of 700 nm corresponding to half the laser frequency. Thus, processes near quarter critical density were not activated in our experiment.

The convective gain of SRS in the backward direction is given by the expression[43,44]

$$G_{SRS} = 1.8 \times 10^{-3} I_{15} L_n \lambda_0, \quad (2)$$

where the characteristic density scale length L_n is in micrometers. According to the hydrodynamic simulations presented in Sec. II, the density scale length is about 50 μm–70 μm at the time 0.5 ns, which is insufficient for excitation of SRS by the heating pulses. After 1 ns, the density scale length increases to 300 μm–500 μm, and the SRS gain for the average N2 beam intensity attains a value of about one. This is

sufficient for SRS excitation in the high-intensity speckles, but not at the average intensity. An increase in the density scale length with time is consistent with the increase in SRS reflectivity with the interaction beam delay.

A typical temporal profile of SRS emission measured with N2 FABS is shown in Fig. 10(b) (green curve) for the case of a 1 ns delay of the N2 beam. It follows the laser pulse shape with a delay ~0.1 ns to 0.2 ns. This small time delay suggests that the cold foam seen by the N2 beam as it enters the target plays a minor role in the interaction process. No notable dependence of SRS signal on the laser beam temporal smoothing or on the foam density was observed. This may be related to a relatively small SSD relative bandwidth of ~3 × 10^{-4}. However, only a small fraction of SRS (3.2 ± 1.2)% goes into the focusing
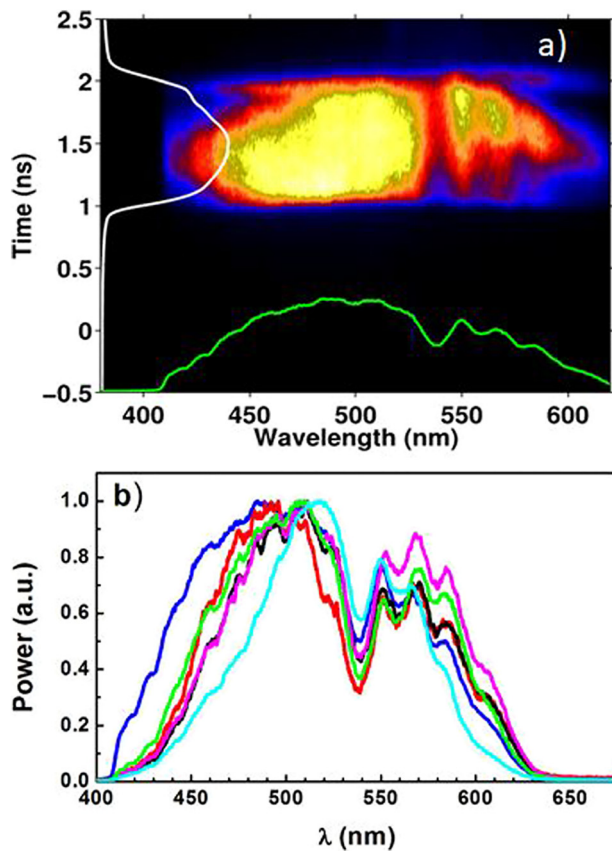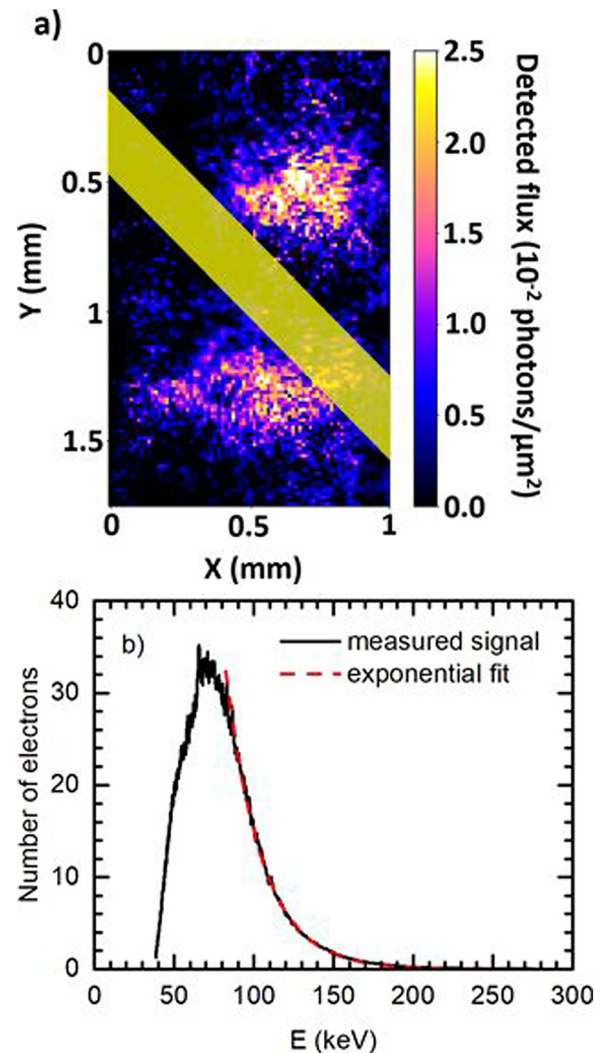

FIG. 11. (a) Time-resolved SRS spectrum of laser light scattered in the N2 FABS below the laser frequency for shot 338. The white and green curves show the time dependence of intensity and the time-integrated spectrum. (b) Time-integrated SRS spectra recorded by the N2 FABS station for shots 338 (blue), 339 (red), 340 (black), 341 (pink), 342 (green), and 344 (cyan). The interaction beam N2 was delayed by 1 ns in all shots, and SSD was turned off in shots 338, 342, and 344. The foam density is 10 mg/cm^3 in shots 338, 339, and 344, and 12 mg/cm^3 in shots 340, 341, and 342. The depressions in the spectra around 530 nm are due to the interference filter suppressing the second harmonic of laser radiation.

FIG. 12. (a) Time-integrated Kα image. The distance between bright spots is ~0.8 mm. The yellow zone shows the projection of the interaction beam. (b) Hot-electron energy distribution measured with the electron spectrometer in the same shot 337 (black). The dashed red curve shows the interpolation with an exponential function corresponding to a temperature of 22 keV.

optics. A much larger fraction of backward SRS, (27.3 ± 3.8)%, was detected by the NBS for the case of a 1 ns delay. A large difference between the SRS signal detected by the FABS and NBS stations is unexpected. This may indicate a significant role of Raman side scattering in our interaction conditions.

In the shots with a 0.5 ns delay of the N2 beam, the SRS signal was delayed by 0.25 ns, with a twice smaller reflected fraction of about (14.0 ± 2.3)%. This may indicate a greater role of cold nonionized foam in the zone where the interaction beam enters the target. This issue needs further analysis.

D. Observation of hot electrons

Generation of hot electrons was diagnosed by electron spectrometers and Kα emission. A typical time-integrated image obtained with Kα x rays is shown in Fig. 12(a) for shot 337. It shows two bright spots at a distance of ~0.8 mm, which is compatible with the target thickness. As the recorded (nonshifted) Kα emission originates from cold atoms with a temperature less than 120 eV,[38] this figure implies that some amount of nonionized foam or cold plasma is present at the target edges. This is confirmed by tracing the N2 beam trajectory over the x-ray image, which passes essentially out of the emission zones. Conversely, by comparing the x-ray emission zones with the beam footprints in Figs. 6(a) and 6(c), one may tentatively attribute their positions to the parts of the foam where no beams are present.

The presence of two spots in the Kα images indicates that the interaction beam propagates throughout the foam from top to bottom, but a small fraction of hot electrons may also be produced by the action of the heating beams. This was confirmed by observation of Kα emission in shot 343, where the N2 beam was absent. However, the action of the N2 beam strongly enhances the Kα emission. A full interpretation of this observation is pending.

Figure 12(b) shows typical time-integrated electron energy distribution measured in one of the ES channels. The electron spectrum can be interpolated with an exponential function corresponding to the hot electron temperature of 22 keV. No electrons with energies above 200 keV have been detected, which is consistent with the hypothesis of their acceleration in the SRS-driven electron plasma waves. It is not, however, possible to estimate the number of produced electrons, because of the small solid angle of reception and the large angle of the spectrometer position with respect to the propagation direction of the interaction beam. Electron spectrometers provide information only on electrons escaping from the target. These represent only a small fraction of the electrons produced by the laser–target interaction. These may be the reasons why the signal from the electron spectrometers varied within two orders of magnitude and did not show any correlation with the measured SRS reflectivity.

The energy range of detected electrons is in qualitative agreement with the process of electron acceleration in the SRS-driven plasma waves. The wavelength range of the SRS spectrum of 450 nm–610 nm corresponds to a range of plasma wave phase velocities $v_{ph} = (0.13–0.30)$ c and a range of energies $\varepsilon_e = m_e v_{ph}^2/2 = 4.5$ keV–25 keV. This range is consistent with the measured temperature of escaped electrons.

The Kα imager was absolutely calibrated and provided us with a number of emitted photons. Assuming isotropic photon emission, the total number of emitted photons varied from ~10^8 in shot 343, where the interaction beam was disabled, to more than 10^{10} in shot 342 showing an SRS reflectivity about 28%. However, that diagnostic was

activated only in six shots, and it was not possible to observe a correlation between the SRS and Kα signals. One may, however, estimate the total number of hot electrons. Considering the copper excitation cross section of 200–300 b and the probability of photon emission ~2×10^{-3}, according to Refs. 49 and 50, one hot electron may produce about 10^{-5} photons while crossing plasma of size 0.5 mm. Thus, a number of emitted photons of 10^{10}, corresponds, according to this estimate, to a total number of hot electrons of about 10^{15}. This number corresponds approximately to 1% of the total number of electrons in a plasma with density 10^{21} cm^{-3} and volume 0.1 mm^3.

V. CONCLUSION AND OUTLOOK

We have studied stimulated scattering of intense laser pulses and hot-electron production in an underdense and hot preformed plasma on the SGIII-P facility. By using a low-density foam target heated by multi-kilojoule laser beams, we succeeded in creating a plasma with a temperature of about 2 keV and a density up to $0.2n_{cr}$ extending over more than a 1000 laser wavelengths. It was shown that such a plasma produces a rather high level of the scattered light in the near-backward direction. Both SBS and SRS contribute on the levels of ~15% and ~30%, respectively, to the plasma reflectivity. While the SBS reflectivity is comparable to the level measured in experiments with gasbags and hohlraums on the same installation,[3] the SRS reflectivity is almost one order of magnitude larger. Such a big difference may be explained by a larger plasma density in our experiment.

It is important to note that for the considered average laser intensity of about 10^{15} W/cm^2 at the third harmonic of the Nd:glass laser, the spatial gains of both scattering instabilities, SBS and SRS, are rather small, of the order of 1–3. A notable amplification is achieved in high-intensity speckles and was not suppressed by SSD. This indicates the importance of implementing laser beam temporal smoothing techniques with a larger bandwidth for controlling the plasma reflectivity. A high level of SRS backscattering is qualitatively correlated with hot-electron generation. However, further development of hot-electron diagnostics is needed for quantitative characterization of the number and spectrum of hot electrons.

Foam targets are promising for detailed studies of parametric instabilities in hot large-scale plasmas. In the numerical simulations, the foam ionization front velocity was overestimated, which resulted in a plasma density limited to $0.2n_{cr}$ and a plasma size limited to 300 μm. Further development of the foam ionization model is needed. This will open the possibility for quantitative design of further experiments with plasmas of a larger size and densities of the order of or larger than the quarter critical density where strong parametric instabilities are expected.

TABLE II. Original data for the scattered energies measured by the FABS and NBS stations.

Shot no.	N2 SBS (J)		N2 SRS (J)		S1 FABS (J)	
	FABS	NBS	FABS	NBS	SBS	SRS
334	54.0	148.5	. . .	83.3	73.1	5.9
335	23.7	96.5	. . .	. . .	80.7	24.3
336	64.6	132.0	. . .	96.6	71.5	3.4
337	89.2	173.4	18.2	123.7	145.8	. . .
338	57.2	136.3	42.9	228.2	145.8	. . .
339	46.5	100.5	15.6	142.0	56.0	. . .
340	67.2	116.7	19.9	167.9	121.1	. . .
341	69.3	85.0	22.2	169.1	95.7	. . .
342	99.8	76.6	38.2	160.4	131.4	. . .
343	. . .	84.0	. . .	. . .	112.9	. . .
344	47.3	113.9	. . .	227.8	107.8	. . .

APPENDIX: ORIGINAL SCATTERED ENERGIES MEASURED IN THE EXPERIMENT

The results recorded by N2 SBS FABS in shots 335 and 343 are used to calculate the energy fraction specularly reflected from beam S2. Based on this fraction, the specular reflection contribution is subtracted in all other shots. Table II presents the reflectivities measured in all channels before subtraction.

REFERENCES

[1]T. Gong, Z. Li, B. Zhao, G.-Y. Hu, and J. Zheng, "Noise sources and competition between stimulated Brillouin and Raman scattering: A one-dimensional steady-state approach," Phys. Plasmas **20**, 092702 (2013).

[2]C. Tian, L. Shan, B. Zhang, W. Zhou, D. Liu, B. Bi, F. Zhang, W. Wang, B. Zhang, and Y. Gu, "Realization of high irradiation uniformity for direct drive ICF at the SG-III prototype laser facility," Eur. Phys. J. D **69**, 54 (2015).

[3]T. Gong, L. Hao, Z. Li, D. Yang, S. Li, X. Li, L. Guo, S. Zou, Y. Liu, X. Jiang, X. Peng, T. Xu, X. Liu, Y. Li, C. Zheng, H. Cai, Z. Liu, J. Zheng, Z. Wang, Q. Li, P. Li, R. Zhang, Y. Zhang, F. Wang, D. Wang, F. Wang, S. Liu, J. Yang, S. Jiang, B. Zhang, and Y. Ding, "Recent research progress of laser plasma interactions in Shenguang laser facilities," Matter Radiat. Extremes **4**, 055202 (2019).

[4]C. Labaune, "Effect of the laser wavelength: A long story of laser-plasma interaction physics for Inertial Confinement Fusion Teller Medal Lecture," EPJ Web Conf. **59**, 01012 (2013).

[5]B. Yaakobi, P.-Y. Chang, C. Stoeckl, A. Solodov, D. H. Edgell, R. S. Craxton, S. X. Hu, J. F. Myatt, F. J. Marshall, W. Seka, and D. H. Froula, "Fast-electron generation in long-scale-length plasmas," Phys. Plasmas **19**, 012704 (2012).

[6]J. F. Myatt, J. Zhang, R. W. Short, A. V. Maximov, W. Seka, D. H. Froula, D. H. Edgell, D. T. Michel, I. V. Igumenshchev, D. E. Hinkel, P. Michel, and J. D. Moody, "Multiple-beam laser–plasma interactions in inertial confinement fusion," Phys. Plasmas **21**, 055501 (2014).

[7]R. K. Follett, J. F. Myatt, J. G. Shaw, D. T. Michel, A. A. Solodov, D. H. Edgell, B. Yaakobi, and D. H. Froula, "Simulations and measurements of hot-electron generation driven by the multibeam two-plasmon-decay instability," Phys. Plasmas **24**, 102134 (2017).

[8]W. Theobald, A. Bose, R. Yan, R. Betti, M. Lafon, D. Mangino, A. R. Christopherson, C. Stoeckl, W. Seka, W. Shang, D. T. Michel, C. Ren, R. C. Nora, A. Casner, J. Peebles, F. N. Beg, X. Ribeyre, E. Llor Aisa, A. Colaïtis, V. Tikhonchuk, and M. S. Wei, "Enhanced hot-electron production and strong-shock generation in hydrogen-rich ablators for shock ignition," Phys. Plasmas **24**, 120702 (2017).

[9]S. Weber, C. Riconda, O. Klimo, A. Heron, and V. T. Tikhonchuk, "Fast saturation of the two-plasmon-decay instability for shock-ignition conditions," Phys. Rev. E **85**, 016403 (2012).

[10]B. B. Afeyan and E. A. Williams, "Unified theory of stimulated Raman scattering and two-plasmon decay in inhomogeneous plasmas: High frequency hybrid instability," Phys. Rev. Lett. **75**, 4218 (1995).

[11]D. Batani, S. Baton, A. Casner, S. Depierreux, M. Hohenberger, O. Klimo, M. Koenig, C. Labaune, X. Ribeyre, C. Rousseaux, G. Schurtz, W. Theobald, and V. T. Tikhonchuk, "Physics issues for shock ignition," Nucl. Fusion **54**, 054009 (2014).

[12]S. Weber and C. Riconda, "Temperature dependence of parametric instabilities in the context of the shock-ignition approach to inertial confinement fusion," High Power Laser Sci. Eng. **3**, e6 (2015).

[13]C. Riconda, S. Weber, V. T. Tikhonchuk, and A. Héron, "Kinetic simulations of stimulated Raman backscattering and related processes for the shock-ignition approach to inertial confinement fusion," Phys. Plasmas **18**, 092701 (2011).

[14]C. Riconda and S. Weber, "Raman–Brillouin interplay for inertial confinement fusion relevant laser–plasma interaction," High Power Laser Sci. Eng. **4**, e23 (2016).

[15]O. Klimo, S. Weber, V. T. Tikhonchuk, and J. Limpouch, "Particle-in-cell simulations of laser-plasma interaction for the shock ignition scenario," Plasma Phys. Controlled Fusion **52**, 055013 (2010).

[16]O. Klimo and V. T. Tikhonchuk, "Laser-plasma interaction studies in the context of shock ignition: The regime dominated by parametric instabilities," Plasma Phys. Controlled Fusion **55**, 095002 (2013).

[17]O. Klimo, J. Psikal, V. T. Tikhonchuk, and S. Weber, "Two-dimensional simulations of laser–plasma interaction and hot electron generation in the context of shock-ignition research," Plasma Phys. Controlled Fusion **56**, 055010 (2014).

[18]Y. J. Gu, O. Klimo, Ph. Nicolaï, S. Shekhanov, S. Weber, and V. T. Tikhonchuk, "Collective absorption of laser radiation in plasma at sub-relativistic intensities," High Power Laser Sci. Eng. **7**, e39 (2019).

[19]S. Depierreux, C. Labaune, D. T. Michel, C. Stenz, Ph. Nicolaï, M. Grech, G. Riazuelo, S. Weber, C. Riconda, V. T. Tikhonchuk, P. Loiseau, N. G. Borisenko, W. Nazarov, S. Hüller, D. Pesme, M. Casanova, J. Limpouch, C. Meyer, P. Di-Nicola, R. Wrobel, E. Alozy, P. Romary, G. Thiell, G. Soullie, C. Reverdin, and B. Villette, "Laser smoothing and imprint reduction with a foam layer in the multikilojoule regime," Phys. Rev. Lett. **102**, 195005 (2009).

[20]S. Depierreux, C. Neuville, C. Baccou, V. Tassin, M. Casanova, P.-E. Masson-Laborde, N. Borisenko, A. Orekhov, A. Colaïtis, A. Debayle, G. Duchateau, A. Héron, S. Hüller, P. Loiseau, Ph. Nicolaï, D. Pesme, C. Riconda, G. Tran, R. Bahr, J. Katz, C. Stoeckl, W. Seka, V. Tikhonchuk, and C. Labaune, "Experimental investigation of the collective Raman scattering of multiple laser beams in inhomogeneous plasmas," Phys. Rev. Lett. **117**, 235002 (2016).

[21]M. J. Rosenberg, A. A. Solodov, J. F. Myatt, W. Seka, P. Michel, M. Hohenberger, R. W. Short, R. Epstein, S. P. Regan, E. M. Campbell, T. Chapman, C. Goyon, J. E. Ralph, M. A. Barrios, J. D. Moody, and J. W. Bates, "Origins and scaling of hot-electron preheat in ignition-scale direct-drive inertial confinement fusion experiments," Phys. Rev. Lett. **120**, 055001 (2018).

[22]K. Nagai, C. S. A. Musgrave, and W. Nazarov, "A review of low density porous materials used in laser plasma experiments," Phys. Plasmas **25**, 030501 (2018).

[23]M. Desselberger, M. W. Jones, J. Edwards, M. Dunne, and O. Willi, "Use of x-ray preheated foam layers to reduce beam structure imprint in laser-driven targets," Phys. Rev. Lett. **74**, 2961 (1995).

[24]S. N. Chen, T. Iwawaki, K. Morita, P. Antici, S. D. Baton, F. Filippi, H. Habara, M. Nakatsutsumi, Ph. Nicolai, W. Nazarov, C. Rousseaux, M. Starodubtsev, K. A. Tanaka, and J. Fuchs, "Density and temperature characterization of longscale length, near-critical density controlled plasma produced from ultra-low density plastic foam," Sci. Rep. **6**, 21495 (2017).

[25]R. J. Mason, R. A. Kopp, H. X. Vu, D. C. Wilson, S. R. Goldman, R. G. Watt, M. Dunne, and O. Willi, "Computational study of laser imprint mitigation in foam-buffered inertial confinement fusion targets," Phys. Plasmas **5**, 211 (1998).

[26]T. Kapin, M. Kuchařík, J. Limpouch, and R. Liska, "Hydrodynamic simulations of laser interactions with low-density foams," Czech J. Phys. **56**, B493 (2006).

[27]S. Yu. Gus'kov, J. Limpouch, Ph. Nicolaï, and V. T. Tikhonchuk, "Laser-supported ionization wave in under-dense gases and foams," Phys. Plasmas **18**, 103114 (2011).

[28]J. Velechovsky, J. Limpouch, R. Liska, and V. Tikhonchuk, "Hydrodynamic modeling of laser interaction with micro-structured targets," Plasma Phys. Controlled Fusion **58**, 095004 (2016).

[29]M. Cipriani, S. Yu. Gus'kov, R. De Angelis, F. Consoli, A. A. Rupasov, P. Andreoli, G. Cristofari, G. Di Giorgio, and F. Ingenito, "Laser-supported hydrothermal wave in low-dense porous substance," Laser Part. Beams **36**, 121 (2018).

[30]M. A. Belyaev, R. L. Berger, O. S. Jones, S. H. Langer, and D. A. Mariscal, "Laser propagation in a subcritical foam: Ion and electron heating," Phys. Plasmas **25**, 123109 (2018).

[31]V. Tikhonchuk, Y. J. Gu, O. Klimo, J. Limpouch, and S. Weber, "Studies of laser-plasma interaction physics with low-density targets for direct-drive inertial conement schemes," Matter Radiat. Extremes **4**, 045402 (2019).

[32]W. Zheng and G. Zhang, "2D hydrodynamic simulation of a line-focused plasma in Ni-like Ag x-ray laser research," Chin. Phys. B **16**, 2439 (2007).

[33]W. Zheng and G. Zhang, "2D simulation of an Ag planar target driven by focus-line laser," Chin. J. Comput. Phys. **25**, 36 (2008), http://www.cjcp.org.cn/EN/abstract/abstract875.shtml.

[34]R. Liska, M. Kuchařík, J. Limpouch, O. Renner, P. Váchal, L. Bednárik, and J. Velechovský, "ALE method for simulations of laser-produced plasmas," Finite Vol. Complex Appl. VI **4**, 857 (2011).

[35]F. J. D. Serduke, E. Minguez, S. J. Davidson, and C. A. Iglesias, "WorkOp-IV summary: Lessons from iron opacities," J. Quant. Spectrosc. Radiat. Transfer **65**, 527 (2000).

[36]R. M. More, K. H. Warren, D. A. Young, and G. B. Zimmerman, "A new quotidian equation of state (QEOS) for hot dense matter," Phys. Fluids **31**, 3059 (1988).

[37]S. Yu. Gus'kov, M. Cipriani, R. De Angelis, F. Consoli, A. A. Rupasov, P. Andreoli, G. Cristofari, and G. Di Giorgio, "Absorption coefficient for nanosecond laser pulse in porous material," Plasma Phys. Controlled Fusion **57**, 125004 (2015).

[38]M. Šmìd, O. Renner, F. Rosmej, and D. Khaghani, "Investigation of x-ray emission induced by hot electrons in dense Cu plasmas," Phys. Scr. **T161**, 014020 (2014).

[39]A. D. Dahl, "SIMION for the personal computer in reflection," Int. J. Mass Spectrom. **3**, 2000 (200).

[40]S. Depierreux, P. Loiseau, D. T. Michel, V. Tassin, C. Stenz, P.-E. Masson-Laborde, C. Goyon, V. Yahia, and C. Labaune, "Experimental investigation of the stimulation Brillouin scatering growth and saturation at 526 and 351 nm for direct drive and shock ignition," Phys. Plasmas **19**, 012705 (2012).

[41]V. Yahia, P.-E. Masson-Laborde, S. Depierreux, C. Goyon, G. Loisel, C. Baccou, N. G. Borisenko, A. Orekhov, T. Rienecker, O. Rosmej, D. Teychenné, and C. Labaune, "Reduction of stimulated Brillouin backscattering with plasma beam smoothing," Phys. Plasmas **22**, 042707 (2015).

[42]P. E. Masson-Laborde, S. Hüller, D. Pesme, Ch. Labaune, S. Depierreux, P. Loiseau, and H. Bandulet, "Stimulated Brillouin scattering reduction induced by self-focusing for a single laser speckle interacting with an expanding plasma," Phys. Plasmas **21**, 032703 (2014).

[43]W. L. Kruer, *The Physics of Laser Plasma Interactions* (Addison-Wesley; CRC Press, Redwood, CA, 1988), ISBN: 978-0367314187.

[44]C. S. Liu, M. N. Rosenbluth, and R. B. White, "Raman and Brillouin scattering of electromagnetic waves in inhomogeneous plasma," Phys. Fluids **17**, 1211 (1974).

[45]H. A. Rose, "Random phase plate hot spots and their effect on stimulated Brillouin backscatter and self-focusing," Phys. Plasmas **2**, 2216 (1995).

[46]V. T. Tikhonchuk, C. Labaune, and H. A. Baldis, "Modeling of a stimulated Brillouin scattering experiment with statistical distribution of speckles," Phys. Plasmas **3**, 3777 (1996).

[47]V. T. Tikhonchuk, Ph. Mounaix, and D. Pesme, "Stimulated Brillouin scattering reflectivity in the case of a spatially smoothed laser beam interacting with an inhomogeneous plasma," Phys. Plasmas **4**, 2658 (1997).

[48]M. Grech, G. Riazuelo, D. Pesme, S. Weber, and V. T. Tikhonchuk, "Coherent forward stimulated-Brillouin scattering of a spatially incoherent laser beam in a plasma and its effect on beam spray," Phys. Rev. Lett. **102**, 155001 (2009).

[49]C. Hombourger, "An empirical expression for K-shell ionization cross section by electron impact," J. Phys. B: At., Mol. Opt. Phys. **31**, 3693 (1998).

[50]A. G. R. Thomas, M. Sherlock, C. Kuranz, C. P. Ridgers, and R. P. Drake, "Hybrid Vlasov–Fokker–Planck–Maxwell simulations of fast electron transport and the time dependance of K-shell excitation in a mid-Z metallic target," New J. Phys. **4**, 015017 (2013).